Full length article

Interfacial thermal conductance between few to tens of layered-MoS$_2$ and c-Si: Effect of MoS$_2$ thickness

Pengyu Yuan [a], Chong Li [a], Shen Xu [a], Jing Liu [a], Xinwei Wang [a, b, *]

[a] 2010 Black Engineering Building, Department of Mechanical Engineering, Iowa State University, Ames, IA, 50011, USA
[b] School of Environmental and Municipal Engineering, Qingdao Technological University, Qingdao, 266033, Shandong Province, PR China

ARTICLE INFO

ABSTRACT

We report a systematic investigation of interfacial thermal conductance (G_k) between few to tens -layered mechanical exfoliated molybdenum disulfide (MoS$_2$) and crystalline silicon (c-Si). Based on Raman spectroscopy, we find G_k at room temperature increases with increased layer numbers of MoS$_2$ from 0.974 MW m^{-2} K^{-1} to 68.6 MW m^{-2} K^{-1}. The higher G_k of thicker samples reveals their better interface contact with the substrate, leading to accordingly improved interfacial energy coupling. Molecular dynamics (MD) simulations are conducted to interpret and compare with the experimental observations. MD simulations predict a thermal conductance in the range of 53–77 MW m^{-2} K^{-1}, which agrees well with the upper bound G_k measured in our work. The thickness dependence of measured G_k reflects the improved interface spacing for thicker MoS$_2$ samples. This phenomenon is further confirmed by the Raman intensity enhancement study by the interface spacing and local optical interference calculations.

1. Introduction

Two-dimensional atomic layer materials, such as graphene, transition-metal dichalcogenides (TMD), have attracted extensive research attention in recent years due to their unique thermal, mechanical, electrical and optical properties [1–3]. Among the layered TMD, MoS$_2$ has been widely used in numerous areas, such as photovoltaic cell [4], nanotribology [5], lithium battery [6], photodetectors [7], memory devices [8], and transistors [9]. For the design and operation of these devices, knowledge of the materials' thermal properties and the interfacial thermal conductance between adjacent layers [10] is a great factor in determining the device performance and durability. Especially, the interface between a two-dimensional atomic layer material and substrate plays a critical role in the overall thermal conductance in the nanosystem and therefore determines the devices' reliability, heat dissipation during operation, and lifetime [11,12]. The thermal transport across interfaces is quantified by the interfacial thermal conductance or Kapitza conductance [13], which is a critical property needed in device thermal design and also an important property to reflect the

local atomic bonding level [14,15]. However, the thermal transport across atomic-layer interfaces is very complicated and challenging to measure since the interfacial thermal conductance is intimately related to the characteristics of the interface properties, such as its structure, bonding, geometry, *etc.* [16–18].

To date, several optical and electrical methods have been employed to measure the interfacial thermal conductance, such as the laser flash method [19], differential 3ω method [20], pump-probe technique [21,22], Raman-based thermal probing technique with electrical heating [23] and laser heating [24]. Particularly, Tang et al. developed a separate laser heating Raman-probe method that has achieved significant improvement in measurement accuracy by controlling the heating with a desired laser wavelength and continuously adjusting the laser energy without interfering the sample [24]. Besides, several theoretical methods were also applied to study the interfacial thermal transport. For example, non-equilibrium molecular dynamics (NEMD) simulation [17,25–27] was a widely used atomistic-scale modeling method for calculating the interfacial thermal conductance. A pump-probe method using molecular dynamics simulation was employed to study the surface roughness effect on thermal transport across the graphene/Si interface [28]. Additionally, the acoustic mismatch model (AMM) [29,30] and diffuse mismatch model (DMM) [31] were also widely used to study the thermal transport across weakly coupled systems

at low temperatures [32].

Extensive research has been done for thermal transport at graphene/substrate interfaces. The results of the interfacial thermal conductance vary greatly due to different graphene preparation methods, the different interface structures, and different substrates. Ruoff et al. in 2009 obtained an interfacial thermal conductance of $(28 + 16/-9.2)$ $MWm^{-2}K^{-1}$ for a supported graphene monolayer grown by chemical vapor deposition on copper [33]. Mak et al. prepared single and multilayered graphene on fused SiO_2 by mechanical exfoliation and obtained the interfacial thermal conductance ranging from 20 to 110 $MWm^{-2}K^{-1}$[34]. Chen et al. designed graphene flakes with different thickness sandwiched between SiO_2 layers and reported the thermal contact resistance from 5.6×10^{-9} to 1.2×10^{-9} Km^2/W with temperatures from 42 to 310 K [35]. In Yue et al.'s work, they obtained the thermal contact resistance between epitaxial graphene and 4H-SiC as high as 5.3×10^{-5} Km^2/W.

As mentioned earlier, knowledge for interface thermal properties of MoS_2 and its substrate is extremely important. Taube et al. prepared a MoS_2 monolayer supported on SiO_2/Si substrates by the mechanical exfoliation method. They obtained an increasing interfacial thermal conductance with increasing temperature from 1.94 $MWm^{-2}K^{-1}$ at 300 K to 1.25 $MWm^{-2}K^{-1}$ at 450 K [36]. In contrast with graphene, little research has been conducted on the thermal transport across the interface between MoS_2 and its substrate. Here we present a detailed temperature and laser power dependent micro-Raman spectroscopy study of different layers MoS_2 nanosheets. We measured the interfacial thermal conductance (G_k) between few to tens of layered MoS_2 and its c-Si substrate. We observed that G_k at room temperature increases with increasing layers of MoS_2. Furthermore, we find that the number of layers (thickness) of MoS_2 deeply affects the film corrugation, morphology, and interfacial thermal conductance. We also conduct MD simulation to better interpret our results.

2. Sample preparation and surface characterization

2.1. Preparation of multilayer MoS_2 nanosheets by mechanical exfoliation method

The layered MoS_2 samples used in our experiments are prepared by micromechanical cleavage of a bulk MoS_2 (429MS-AB, molybdenum disulfide, small crystals from USA, SPI Suppliers). Several methods have been reported to prepare atomically thin MoS_2 nanosheets, such as chemical vapor deposition and liquid exfoliation, etc. Among these, mechanical exfoliation is widely used and the most efficient way to produce clean, highly crystalline and atomically thin nanosheets of layered materials for investigating of their intrinsic thickness-dependent properties [37]. As in the typical mechanical exfoliation process, we first put a small piece of bulk MoS_2 on the sticky side of a piece of ordinary adhesive Scotch tape and then peel off appropriate thin MoS_2 crystals. After repeating the peeling process several times, we identify some relatively thin crystals on the Scotch tape with microscope. Then we lay one gel film (Gel-Film, PF-20/1.5-X4, Gel-Pak) on the crystals and gently rubbed the back of the gel film by using tools such as a plastic plate to further cleave the crystals. The third step is to quickly peel back the gel film from the Scotch tape to transfer the crystals. Then we apply crystals inked gel film to a freshly cleaned c-Si substrate and carefully rub the back of gel film again. At last, by slowly peeling off the gel film from the substrate, several MoS_2 nanosheets with different thickness are left there [38]. The size of layered MoS_2 nanosheets ranges from 3 to 15 μm. Optical microscope (Olympus BX53), atomic force microscope (AFM) and Raman spectroscopy are used to locate the MoS_2 nanosheets.

2.2. Surface morphology and layer thickness study using AFM

Fig. 1 shows AFM images of seven cleaved samples of multilayer MoS_2 nanosheets. AFM is also used to measure the thickness of these MoS_2 samples. We choose the contact mode of AFM instead of tapping or other modes to avoid possible artifacts in the nanosheet thickness measurements [39]. Because currently we do not have the technique for sample thickness control, there is only one sample for each thickness level. The measurement uncertainty has been carefully evaluated and presented with the reported results. In Fig. 1, for each sample, the left figure gives the 2D contour. The MoS_2 sample is marked by the white dashed curves. The two blue lines indicate the edges where the height is measured [shown in the figures in the middle, e.g. Fig. 1(a-1) and Fig. 1(a-2)]. The blue dashed square indicates the location for detailed MoS_2 surface morphology study. This morphology study is shown in the top figure on the right, e.g., Fig. 1(a-3). The bottom figure on the right [e.g., Fig. 1(a-4)] shows the height variation along the blue line in the top figure on the right [e.g., Fig. 1(a-3)].

Take the AFM image of the 45 nm-thick sample as an example [Fig. 1(a)], we explain the surface morphology characterization results. We can find that the surface height varies as much as 9.5 nm which indicates the existence of corrugations and/or ripples on the MoS_2 layers [Fig. 1(a-4)]. This variation is also partly induced by the non-uniform layer number of the sample. For other six samples, the surfaces are found much smoother with a height measurement noise of around 0.3 nm. The average height variation ranges from 0.94 nm to 0.43 nm and the surface becomes smoother for thinner MoS_2 samples. The noise in the AFM measurement (~0.5 nm) is obvious for the 4.2 nm thick sample and the white spots in Fig. 1(d, f) are residual from gel films. In the experiment, the laser spot is on the MoS_2 sample completely. From all the figures, it is conclusive that the surface of MoS_2 sample is atomically smooth, except for the first sample (45 nm). In Fig. 1(f), we can find that on the large sample there are also some small flakes. The large MoS_2 sample has a thickness of 5 nm [Fig. 1(f-1) and 1(f-2)]. The surface of the substrate we use is the same as that used in Tang et al.'s work [24]. As shown in Fig. 3(b) of his work, when considering the AFM measurement noise, the surface of the c-Si is very flat (~0.3 nm) and shows no protruding points on it. In our interface characterization, the laser spot is focused on the area without extra flakes, like the area indicated by the dashed square.

3. Experimental design and physical model for interface characterization

3.1. Experimental setup

Raman scattering studies are conducted by using a BWTEK Voyage confocal Raman microscope system using a longitudinal single mode laser with an excitation wavelength of 532 nm as shown in Fig. 2(a). The laser is introduced to the Raman system and its energy is adjusted by a neutral-density (ND) filter. Search and identifying of the MoS_2 nanosheet sample on c-Si under microscope is realized using a 3D nano-stage (MAX313D, Thorlabs, Inc.) with a resolution of 5 nm. The laser beam is focused on the center of the sample and the laser power is varied between 2.61 mW and 12.12 mW to introduce different heating levels in the MoS_2 samples. The absorbed energy is conducted away across the MoS_2/c-Si interface to the substrate. We use the Raman spectrometer to measure the temperature of MoS_2 and c-Si simultaneously. Based on the temperature difference between MoS_2 and c-Si, and the absorbed laser power, we can directly determine the interfacial thermal conductance. Shown in Fig. 2(b) (c) are the laser energy distribution (contour and 3D) under a 20 × objective lens. From
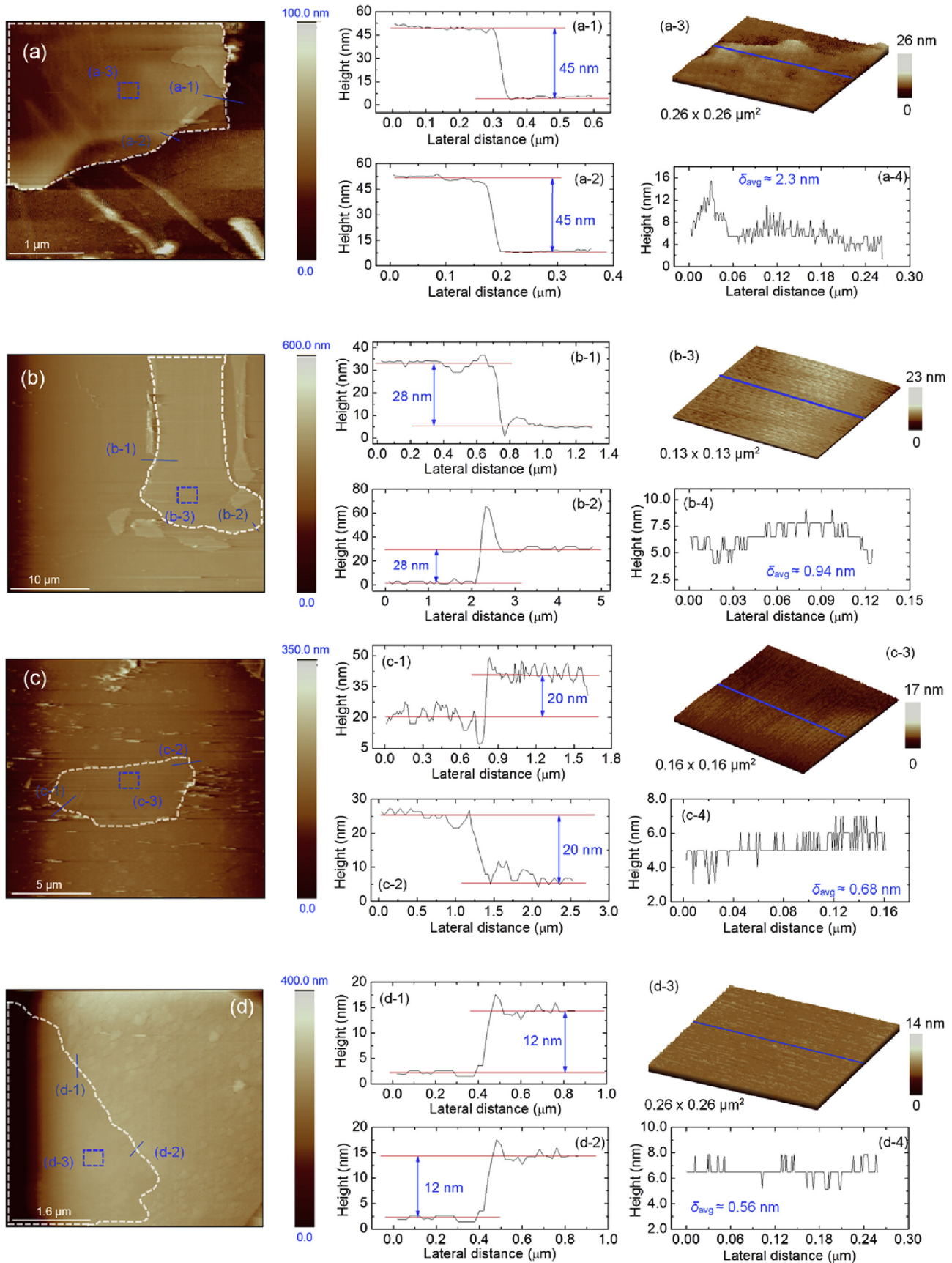
Fig. 1. Sample thickness measurement and surface characterization. (a)–(g) AFM images of the MoS_2 nanosheets. The white dashed box indicates the MoS_2 sample area. The middle two figures [e.g. (a-1) and (a-2)] in each panel show the step height measurement results from the substrate to the sample. The measurement is along the blue lines in the left figure. The upper right figure [e.g. (a-3)] shows the AFM 3D mapping of the MoS_2 on c-Si over the over marked by the blue dashed box in the left figure. The last figure [e.g. (a-4)] shows the sample surface height variation along the blue line in its top figure [e.g. (a-3)]. (For interpretation of the references to colour in this figure legend, the reader is referred to the web version of this article.)
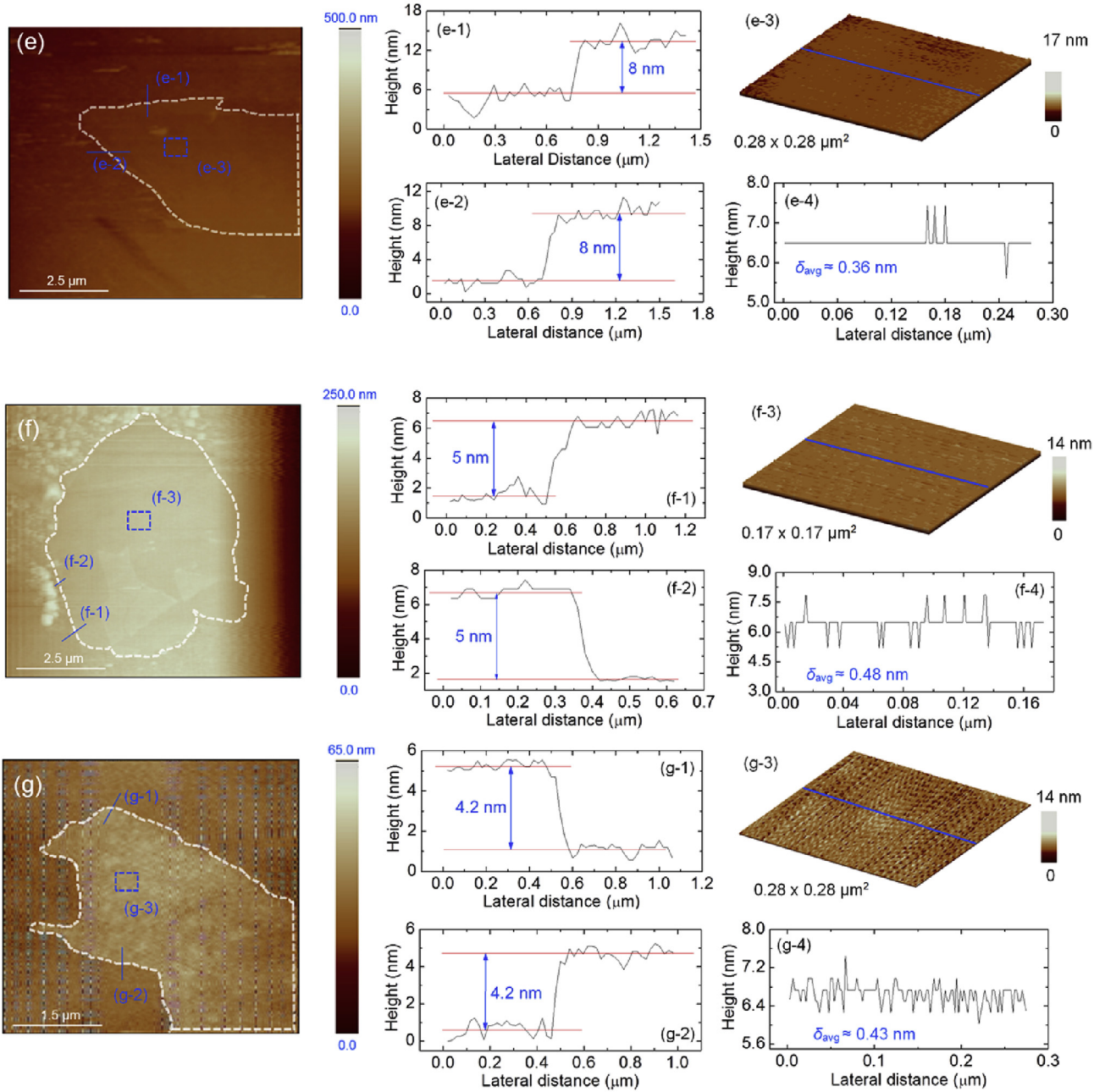
Fig. 1. (*continued*).

Fig. 2(c) is clear that the energy distribution can be well described by a linear line from the center of the spot to its edge. Under 20 × , the spot size is around 5 μm. Under 50 × , the spot size is around 1.9 μm. Quantitative definition of the spot size depends on how it is evaluated. Below when we discuss the physical model, the spot size will be discussed more. Physical models for detailed data processing will be described below, too. In our experiment, depending on the sample size and thickness, either 20 × or 50 × objectives is used. Details are summarized in Table 1.

3.2. Effective thermal conductance between MoS₂ and c-Si

Considering the non-uniform distribution of the laser energy in space [Fig. 2(b) and (c)], the temperature distribution in the MoS₂ nanosheet measured in the experiment could be obtained from following heat diffusion equation in the cylindrical coordinate:

$$k_s t \frac{1}{r} \frac{d}{dr}\left(r\frac{dT}{dr}\right) - G_e(T_1 - T_2) + I_a = 0, \tag{1}$$

where G_e is the effective interfacial thermal conductance per unit area. T_1 is the temperature rise of MoS₂ nanosheet upon laser heating, T_2 the temperature rise of c-Si. Note the effective interfacial thermal conductance (G_e) is defined based on the effective/average temperature measured in the experiment: T_1 and T_2. Since the measured temperatures do not represent the temperature of MoS₂ and c-Si at locations immediately adjacent to their interface, the effect of temperature distribution in the thickness direction for MoS₂ and c-Si will be considered to find the true interfacial thermal conductance. I_a (W/m²) represents the absorbed laser power per
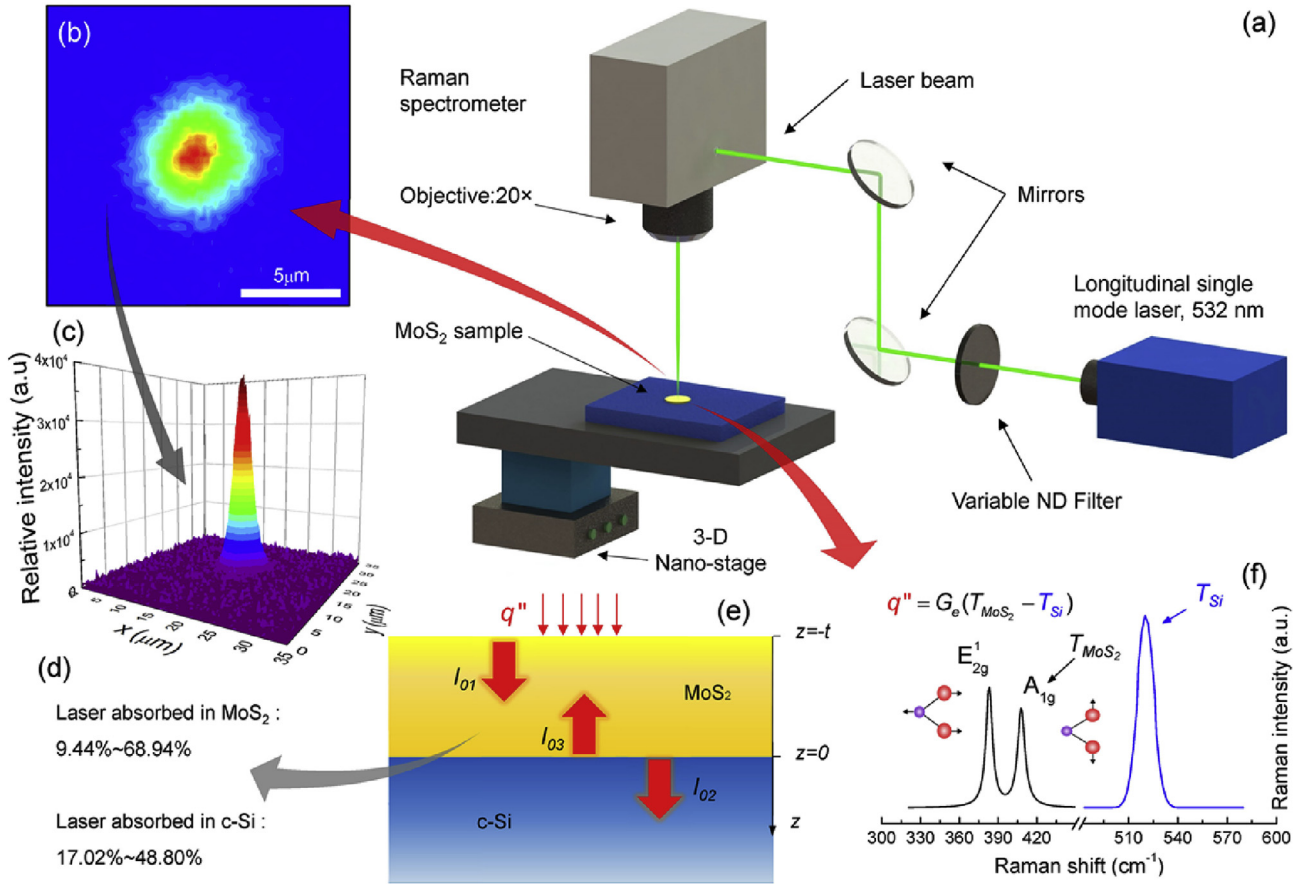
Fig. 2. Schematic of the experimental setup for characterizing the MoS$_2$/c-Si interface energy coupling. (a) A typical MoS$_2$/c-Si sample is heated up by the continuous wave 532 nm green laser light. The Raman signals of MoS$_2$ and c-Si are excited by the same laser and collected by a confocal Raman spectrometer (Voyage, B&W Tek, Inc.) with a spectral resolution of 1.05–1.99 cm^{-1}. The position of the sample is controlled by a 3D nano-stage with a resolution of 5 nm. The MoS$_2$ flakes absorb laser energy and dissipate heat to the c-Si substrate through their interface. (b) (c) The spatial energy distribution of the laser beam. The laser spot size on the sample is roughly given as: 35.7 μm^2 under 20 × objective, and 5.90 μm^2 under 50×. (d) (e) When laser beam irradiates the sample surface, multiple reflections happen at the interface between MoS$_2$ and c-Si. The transmitted power at the top surface (I_{01}), the transmitted power in c-Si top surface (I_{02}) and the reflected power at the bottom surface (I_{03}) of MoS$_2$ are calculated out according to the transfer Matrix Method (TMM) [40]. The laser energy absorbed in MoS$_2$ varies from 9.44% to 68.94% and absorbed in c-Si from 17.02% to 48.80% for different layered MoS$_2$ samples from 75 layers to 7 layers when considering the multiple reflections. (f) Temperatures of both MoS$_2$ and c-Si can be determined simultaneously by one Raman spectrum. Here we choose the A$_{1g}$ mode of MoS$_2$ to determine its temperature. (For interpretation of the references to colour in this figure legend, the reader is referred to the web version of this article.)

Table 1
Temperature coefficient of different layered MoS$_2$ nanosheets and c-Si under the corresponding objective lens, and interfacial thermal conductance between different layered MoS$_2$ and c-Si based on Raman properties of the A$_{1g}$ Mode.

Layer number of MoS$_2$, objective lens	G_k by Raman parameters of A$_{1g}$ mode (MW/m^{2}K)	Temperature coefficient χ_T (cm^{-1}/K)		
		A$_{1g}$ mode	E$^1_{2g}$ mode	c-Si
7 L, 50 × lens	0.974 ± 0.158	−(0.0143 ± 0.0005)	−(0.0146 ± 0.0004)	−(0.0191 ± 0.0017)
8 L, 20 × lens	1.05 ± 0.172	−(0.0110 ± 0.0005)	−(0.0111 ± 0.0004)	−(0.0195 ± 0.0018)
13 L, 20 × lens	6.00 ± 1.46	−(0.0153 ± 0.0014)	−(0.0158 ± 0.0008)	−(0.0190 ± 0.0010)
20 L, 20 × lens	7.58 ± 1.06	−(0.0237 ± 0.0013)	−(0.0299 ± 0.0019)	−(0.0248 ± 0.0011)
33 L, 20 × lens	17.5 ± 3.02	−(0.0174 ± 0.0013)	−(0.0221 ± 0.0275)	−(0.0271 ± 0.0004)
47 L, 20 × lens	21.0 ± 3.68	−(0.0221 ± 0.0013)	−(0.0275 ± 0.0015)	−(0.0353 ± 0.0016)
75 L, 50 × lens	68.6 ± 9.14	−(0.0174 ± 0.0010)	−(0.0194 ± 0.0012)	−(0.0355 ± 0.0006)

unit area in MoS$_2$. This is calculated according to the TMM [40]. The refractive index of air is 1. The refractive index and extinction coefficient of MoS$_2$ are taken as 5.2 and 1.1 when the wavelength (λ) of the laser beam is 532 nm [41]. The refractive index and extinction coefficient of c-Si are 4.15 and 0.05 when λ is 532 nm [24]. k_s=52 Wm^{-1}K^{-1} is the in-plane thermal conductivity of MoS$_2$ nanosheet [42]. r is the radial position measured from the center of the laser beam, r_0 the radius of the laser beam spot, and t the MoS$_2$ nanosheet thickness. In our experiment, the measured temperature rise

is Raman/laser intensity weighted average over the laser spot size and can be expressed as

$$\bar{T} = \int_0^{r_0} I_a T dA \Big/ \int_0^{r_0} I_a dA. \tag{2}$$

To reflect this weighted average temperature in above equation, we multiply I_a on both sides of Eq. (1), do the integral over the laser spot area, and then divide them by $\int_0^{r_0} I_a dA$, finally we have

$$\frac{k_s t}{Q} I_{a(\max)} \overline{T_1} - G_e\left(\overline{T_1} - \overline{T_2}\right) + \int_0^{r_0} I_a^2 dA \Big/ \int_0^{r_0} I_a dA = 0. \qquad (3)$$

Here $I_{a(max)}$ is the absorbed laser intensity in the center of the laser spot. In the above integral, we take one assumption that at the edge of the laser spot, the temperature rise is much smaller than the average temperature rise. This is true since the sample is very thin, the heat conduction/transfer along the thickness direction in MoS$_2$ is much larger than that in the in-plane direction. In the above equation, the term $\int_0^{r_0} I_a^2 dA / \int_0^{r_0} I_a dA$ in fact gives an equivalent heat flux (q_{eff}'') we can obtain from our laser beam distribution and use it to evaluate G_e. Fig. 2(b) and (c) show the contour and 3D profile of the laser beam for non-uniform laser distribution in space. Based on the calculated effective laser energy density, we could further evaluate the laser beam size as $A_{beam} = (\int I_a dA)^2 / \int I_a^2 dA$. Using this definition, the spot size is calculated as 35.7 μm^2 for 20 × and 5.90 μm^2 for 50 × . In our experiment, q_{eff}'' for different laser energy levels are evaluated and used to suppress experimental noise and determine the interfacial thermal conductance.

As shown in Fig. 2(b) and (c), the laser intensity can be well represented with a linear distribution from the spot center to its edge. Therefore, we can calculate the total absorbed laser power Q in Eq. (3) as

$$Q = \int_0^{r_0} 2\pi I_a r dr = \int_0^{r_0} I_{a(\max)}\left(1 - \frac{r}{r_0}\right) 2\pi r dr = \frac{I_{a(\max)}}{3}\pi r_0^2. \qquad (4)$$

Finally, the effective interfacial thermal conductance can be described as

$$G_e = \frac{3k_s t/(\pi r_0^2) \cdot \overline{T_1} + q_{eff}''}{\overline{T_1} - \overline{T_2}}. \qquad (5)$$

In the experiment, by using only one incident laser energy, we can measure $\overline{T_1}$, $\overline{T_2}$ and q_{eff}'', and then determine G_e. To suppress the experimental noise, we use different incident laser energy levels, and plot how $\overline{T_1}$ and $\overline{T_2}$ linearly vary against q_{eff}''. Instead of using their absolute value, the slope of the relation: $\partial \overline{T_1}/\partial q_{eff}''$ and $\partial \overline{T_2}/\partial q_{eff}''$ are used to determine the effective thermal conductance as

$$G_e = \frac{3k_s t/(\pi r_0^2) \cdot \partial \overline{T_1}/\partial q_{eff}'' + 1}{\partial \overline{T_1}/\partial q_{eff}'' - \partial \overline{T_2}/\partial q_{eff}''}. \qquad (6)$$

The quantity $\partial \overline{T}/\partial q_{eff}''$ could be experimentally obtained using following relation:

$$\frac{\partial \overline{T}}{\partial q_{eff}''} = \frac{\partial \omega}{\partial q_{eff}''} \Big/ \frac{\partial \omega}{\partial T} = \frac{q_{eff}''}{P}\chi_p\chi_T^{-1}, \qquad (7)$$

where χ_T and χ_p is first-order temperature coefficient and power coefficient for the Raman shift of MoS$_2$ and c-Si. P is the laser power reaching the sample surface. The temperature coefficients of the Raman shift are obtained from the separate temperature calibration experiments. In our experiment, 8 different incident laser powers are introduced to achieve accurate and linear power coefficients for MoS$_2$ and c-Si.

3.3. Evaluation of the real interfacial thermal conductance

In our experiment, as mentioned before, the measured temperatures of MoS$_2$ and c-Si are not the ones immediately adjacent to their interface. Rather they have the effect of the temperature distribution in the thickness direction for both MoS$_2$ and c-Si, and are discussed as below.

Considering the finite thickness of MoS$_2$, there is a temperature gradient existing in MoS$_2$ caused by the exponential laser energy absorption and heat conduction in the MoS$_2$ nanosheet. The penetration depth of the Raman laser in MoS$_2$ is $\tau_1 = \lambda/(4\pi\kappa_{MoS2})$. At $\lambda = 532$ nm, the extinction coefficient κ_{MoS2}=1.1 for MoS$_2$, we have τ_1=38.5 nm. As shown in Fig. 2(e), we could describe the energy absorbed in MoS$_2$ nanosheets within $(-t, z)$ as $I_{MoS_2}(z) = I_{01}[1 - e^{-(z+t)/\tau_1}]$ following the coordinate definition in Fig. 2(e). In our work, since the sample is very thin, the heat conduction in the thickness direction is dominant over that in the in-plane direction. Also as indicated in Fig. 2(e), the reflected laser beam at the MoS$_2$/c-Si interface is negligible in MoS$_2$ in terms of absorption from the multiple reflections calculation. As a result, the temperature distribution within MoS$_2$ could be expressed as $T_1(z) = T_1|_{z=0} + \int_{-t}^0 I_{01}/k_{s'}[1 - e^{-(z+t)/\tau_1}]dz$, where I_{01} is the laser intensity just entering MoS$_2$ from the top surface [Fig. 2(e)]. $k_{s'}$ is the cross-plane thermal conductivity of MoS$_2$ nanosheets which has been obtained as 2 W m^{-1}K^{-1}[43]. Actually, the Raman-based temperature measurement is an intensity-weighted average temperature in the thickness direction. So $T_{exp}' = \int_{-t}^0 T_1(z)e^{-(z+t)/(\tau_1/2)}dz/\int_{-t}^0 e^{-(z+t)/(\tau_1/2)}dz = T_1|_{z=0} + f_1(t)I_{01}$. $f_1(t)$ is a function of thickness t and given as:

$$f_1(t) = \frac{\tau_1\left(-2e^{-3t/\tau_1} + 3e^{-2t/\tau_1} + 6e^{-t/\tau_1} - 7\right) + 6t}{6k_{s'}\left(1 - e^{-2t/\tau_1}\right)}. \qquad (8)$$

The equivalent heat conduction resistance (R_1) caused by the finite thickness is

$$R_2 = \frac{\int f_1(t)I_{01}I_a dA \Big/ \int I_a dA}{[3k_s t/(\pi r_0^2)]\cdot\overline{T_1} + q_{eff}''} = \frac{f_1(t)\cdot q_{eff}''\Big/\left(1 - e^{-t/\tau_1}\right)}{[3k_s t/(\pi r_0^2)]\cdot\overline{T_1} + q_{eff}''}. \qquad (9)$$

For c-Si, similar to MoS$_2$, its measured temperature is not the temperature immediately next to its upper surface either, but an average temperature within the focal depth of the Raman probing laser. The temperature distribution reflects the effects of the heat flux from the MoS$_2$ sheet plus the laser energy absorption in c-Si. The temperature rise distribution induced by the heat flux from MoS$_2$ is linearly distributed against the thickness in the region close to the c-Si surface. The penetration depth of the Raman laser in c-Si is $\tau_2 = \lambda/(4\pi\kappa_{Si})$. With κ_{Si}=0.05 for silicon, we have τ_2=820 nm. As the Raman excitation laser is focused on the c-Si surface and considering the Raman intensity weighted average for temperature measurement, we can calculate the measured temperature of c-Si as $T_{exp} = \int_0^\infty T_2(z)\cdot e^{-z/(\tau_2/2)}dz/\int_0^\infty e^{-z/(\tau_2/2)}dz = T_2|_{z=\tau_2/2}$[24], where z is the distance from c-Si surface as shown in Fig. 2(e). This means the extra temperature of c-Si measured in the experiment is equal to the value at $z = \tau_2/2 = 410$ nm. The equivalent heat conduction resistance of c-Si across this distance is $R_2 = \tau_2/\{2k_{Si}[3k_s t/(\pi r_0^2)\cdot\partial\overline{T_1}/\partial q_{eff}'' + 1]\}$, which we should subtract from the measured effective thermal resistance (G_e^{-1}).

Finally, the laser energy transmitted from MoS$_2$ nanosheets to c-Si also causes a temperature gradient in c-Si because of the laser beam absorption in it. As shown in Fig. 2 (e), the energy absorbed in c-Si within $(0, z)$ could be described as $I(z) = I_{02}(1 - e^{-z/\tau_2})$ and the temperature distribution could be expressed as $T_2(z) = T_2|_{z=0} - \int_0^z I_{02}/k_{Si}(1 - e^{-z/\tau_2})dz$. Here I_{02} is the laser

intensity just entering c-Si from the interface, and is expressed as $I_{02}(1 - e^{-t/\tau_2})$ after neglecting the weak reflection at the local interface. Similar to MoS_2, the Raman-based temperature measurement in c-Si is also an intensity-weighted temperature for the laser spot. So this effect is expressed as $T'_{exp} = \int_0^\infty T_2(z) \cdot e^{-z/(\tau_2/2)} dz / \int_0^\infty e^{-z/(\tau_2/2)} dz = T_2|_{z=0} - I_{01}(1 - e^{-t/\tau_1})\tau_2/6k_{Si}$. The equivalent heat conduction resistance caused by this effect is

$$R_3 = \frac{\int \left[I_{01}\left(1 - e^{-t/\tau_1}\right)\tau_2 \big/ (6k_{Si}) \cdot I_a \right] dA \big/ \int I_a dA}{3k_s t / (\pi r_0^2) \cdot \overline{T_1} + q''_{eff}}$$

$$= \frac{q''_{eff}\tau_2}{6k_{Si}\left[3k_s t / (\pi r_0^2) \cdot \overline{T_1} + q''_{eff}\right]}. \tag{10}$$

To the end, the real interfacial thermal conductance G_k should be:

$$G_k = \frac{3k_s t / (\pi r_0^2) \cdot \overline{T_1} + q''_{eff}}{T_1|_{z=0} - T_2|_{z=0}} = \frac{1}{G_e^{-1} - R_1 - R_2 - R_3}. \tag{11}$$

4. Results and discussion

4.1. Raman characterization of layered MoS_2 nanosheets

For all the seven MoS_2 samples, first of all, we conduct Raman characterization under the same conditions to study the sample's difference in terms of Raman properties. A 532 nm laser is used in the Raman spectroscopy study. And we use a $50 \times$ objective lens to focus the laser light and collect the Raman signal. The samples are excited with 3.28 mW laser power and integrated for 10 s. Fig. 3(a) shows the strong signals from both E_{2g}^1 and A_{1g} vibration modes in ambient environment. The E_{2g}^1 mode is associated with in-plane opposite vibration of two sulfur atoms with respect to the molybdenum atom, whereas the A_{1g} mode is associated with out-of-plane vibration of only sulfur atoms in opposite directions [36]. We observe the E_{2g}^1 (~383 cm^{-1} for thin MoS_2) and A_{1g} (~407 cm^{-1} for thin MoS_2) modes from curve fitting by using the Lorentzian function. Instead of using Gaussian function, we find using Lorentzian function could better determine the Raman parameters of MoS_2. Fig. 3(b) depicts the Gaussian-fit Raman spectra of c-Si with different thickness MoS_2 nanosheets on its surface. The c-Si Raman peak position at around 521 cm^{-1} determined from the Gaussian fit is used as an intrinsic Raman shift for temperature determination of the c-Si substrate. As shown in Fig. 3(c), we could observe the thickness dependence of the Raman intensity of Raman active E_{2g}^1 and A_{1g} modes in MoS_2 nanosheets. When the sample is thicker, the Raman signal of MoS_2 is stronger and that of c-Si is weaker (inset). For the Raman intensity of MoS_2, it does not increase with the sample thickness linearly since the laser absorption in MoS_2 follows an exponential function. The trend indicates that when the thickness of MoS_2 goes further, intensity saturation will be reached. For the Raman intensity of c-Si, when the MoS_2 layer is thicker, less laser will reach the substrate to excite Raman signals. Also less percentage of the Raman signal will have the chance to reach out and be detected due to the fact that some Raman signal is also absorbed by MoS_2 nanosheets.

Fig. 3(d) displays the thickness dependence of Raman shift of two Raman modes in MoS_2 nanosheets. The Raman shift of E_{2g}^1 mode softens while that of the A_{1g} mode has a blue shift with the increased layer number. These are mainly due to the fact that the interlayer Van der Waals force in MoS_2 layers becomes stronger

with increased layer number, causing the decrease of the force constant for A_{1g} mode and structure changes. As for the contrary behavior in E_{2g}^1 mode of MoS_2, it suggests that the increased interlayer Van der Waals force may play a minor role. The stacking induced structure change or the possible presence of additional interlayer interactions such as the long-range Coulomb interlayer interactions in layered MoS_2 nanosheets may dominate the change of atomic vibration. We also plot the Raman shift difference [$(\Delta\omega = \omega(A_{1g}) - \omega(E_{2g}^1)$, in cm^{-1} unit] as a function of the layer number. The result is shown in Fig. 3(d). We can find that this difference increases with the layer number of MoS_2. In the past, the Raman shift difference has been found to be a convenient diagnostic of the layer thickness of MoS_2 nanosheets. Our result is consistent with results and predictions of *Lee* et al.'s work: $\Delta\omega = 25$ cm^{-1} is for about 7 layers and $\Delta\omega$ increases with increasing sample thickness [44].

4.2. Interfacial thermal conductance characterization

In our interfacial thermal conductance experiments, for each sample, 8 room-temperature Raman spectra are collected at the laser power ranging from 2.61 to 12.12 mW. This heating power variation is designed to study the Raman spectrum change under the heating and to significantly suppress the noise. Fig. 4(a) shows the five representative Raman spectra and their corresponding Lorentzian fits collected from the MoS_2 sample of 4.2 nm thickness. As the laser power increases, the Raman wave number of both E_{2g}^1 and A_{1g} modes shift to left (red-shift). These changes indicate the local temperature of the sample surface goes higher under a higher laser power. The Raman shift for the two vibration modes as a function of incident laser power are plotted in Fig. 4(c). In our specified laser power range, it is observed that the Raman shift linearly depends on the laser power by $\Delta\omega = \omega(P_2) - \omega(P_1) = \chi_P(P_2 - P_1) = \chi_P\Delta T$. χ_P is the first-order laser power coefficient for MoS_2 vibration mode and P is the laser power. The fitted χ_P for E_{2g}^1 and A_{1g} modes are quite close, $-(0.182 \pm 0.010)$ cm^{-1}/mW and $-(0.192 \pm 0.012)$ cm^{-1}/mW, respectively.

We also calibrate the temperature coefficients of MoS_2 and c-Si Raman spectra to determine the local temperature during the interfacial thermal conductance experiment. This calibration is conducted for each sample considering the possible sample-to-sample difference. In the calibration experiments, the MoS_2/c-Si sample is placed on a heated stage and the sample's temperature is controlled by a voltage transformer that powers the heater, and monitored by a thermocouple. Raman spectra of both MoS_2 and c-Si are collected after the sample's temperature reaches a stable reading. Fig. 4(b) shows four representative Raman spectra and their corresponding Lorentzian fits with the temperature ranging from 310 to 415 K. The Raman shift of both E_{2g}^1 and A_{1g} modes decreases against increased temperature. Fig. 4(d) shows the temperature coefficients of the Lorentzian-fit Raman peaks from 292 to 415 K for both E_{2g}^1 and A_{1g} modes. At higher temperatures, all layers expand with the same rate leading to a nearly linear decrease of the Raman shift for both E_{2g}^1 and A_{1g} modes. So that we could describe the Raman peak position as a function of temperature $\Delta\omega = \omega(T_2) - \omega(T_1) = \chi_T(T_2 - T_1) = \chi_T\Delta T$. χ_T is the first-order temperature coefficient for MoS_2 vibration modes and T is temperature. Here, we do not consider the higher order temperature coefficients because these terms are significant only at high temperature about 570 K and above [42,45]. In our experiment, the MoS_2/c-Si samples are firmly placed on the 3D nanostage and the same point of each sample is measured during temperature calibration and interfacial thermal conductance experiment. This treatment eliminates possible location-to-location structure variation and temperature coefficient variation.
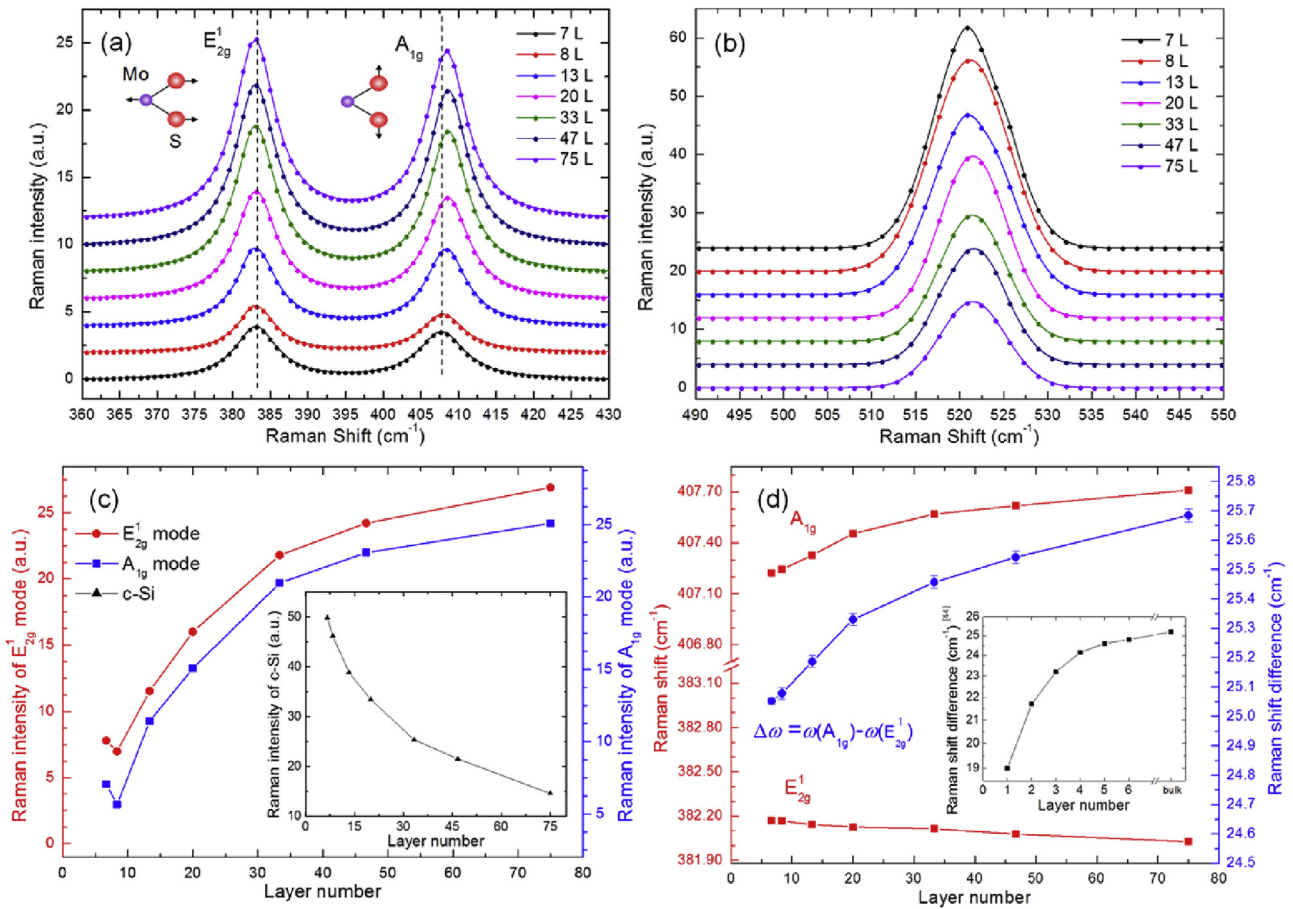
Fig. 3. Raman characterizations of seven MoS$_2$ nanosheet samples. A 532 nm laser is used to examine the thickness-dependence of the MoS$_2$ Raman spectra. (a) The Lorentzian-fit Raman spectra of 7 layers to 75 layers (7 L-75 L) MoS$_2$ nanosheets taken with a 50 × objective lens. The samples are excited with 3.28 mW laser power and integrated for 10 s. (b) The Gaussian-fit Raman spectra of c-Si with different layered MoS$_2$ nanosheets recorded simultaneously with those shown in (a). The Raman spectra are shifted vertically to distinguish them in these two figures. (c) Thickness dependence of the Raman signal intensity of Raman active E_{2g}^1 (in-plane) and A_{1g} (out-of-plane) modes in MoS$_2$ nanosheets. The inset shows that when the sample is thicker, the Raman signal of c-Si is weaker. (d) Thickness dependence of Raman shift of two Raman modes in MoS$_2$ nanosheets (left vertical axis) and their difference (right vertical axis). The two modes shift away from each other with increasing thickness. The inset shows the results and predictions based on *Lee* et al.'s work [44].

The observed linear evolution of the Raman peak position with temperature is actually a manifestation of the anharmonic terms in the lattice potential energy which is determined by the phonon occupation number, the anharmonic potential energy, and the thermal expansion of the crystal. That is, the temperature effects could be approximately attributed to two factors: energy shift of the lattice due to the anharmonic phonon-phonon interactions and the shift contribution caused by the thermal expansion of the crystal. As the lattice expands or contracts because of temperature change, the equilibrium positions of atoms are displaced and consequently the interatomic forces change. This modifies the phonon vibrational frequencies shown in the form of the Raman spectra [46]. In our work, the temperature coefficients difference of vibration mode E_{2g}^1 and A_{1g} shown in Fig. 5(a) as red and blue curves are just an indication of the different anharmonic coupling of the phonon modes. Because we prepare all the MoS$_2$ nanosheets samples by mechanical exfoliation, it is highly possible that wrinkles and/or ripples are introduced to the nanosheets which could result stress/strain in the nanosheets. Additionally, the MoS$_2$ nanosheets on c-Si substrate could be more affected by the changes in the nanosheets morphology such as wrinkles and ripples when temperature increases. This is mainly caused by the thermal expansion coefficient difference between MoS$_2$ and c-Si. All these combine together to result in different temperature coefficients

among MoS$_2$ samples as shown in Fig. 5(a) and Table 1.

Based on the first-order temperature coefficient χ_T and the power coefficient χ_P for MoS$_2$, we could extract the interfacial thermal resistance/conductance between MoS$_2$ and c-Si as shown in Fig. 5(b), (c), and (d). From Fig. 5(b, c), we can find that the three temperature correction equivalent thermal resistances together have bigger effects on interfacial thermal resistance (G_k^{-1}) when the sample is thicker. R_2 is roughly a constant. R_3 approaches zero while R_1 becomes larger for thicker samples. And the equivalent heat conduction resistance (R_1) caused by the finite thickness of MoS$_2$ affects G_k^{-1} most. By subtracting all those three equivalent thermal resistances, we get that G_k^{-1} decreases by about two orders of magnitude with increasing layer numbers of MoS$_2$ based on the Raman parameters of both E_{2g}^1 and A_{1g} vibration modes. From Fig. 5(d), G_k obtained from E_{2g}^1 and A_{1g} vibration modes are very close and follow the similar trend. Since the E_{2g}^1 mode would be more affected by the interaction between the nanosheets and the substrate than the A_{1g} mode [45], we choose the A_{1g} mode results to evaluate the interfacial thermal conductance and elaborate the discussion. The uncertainty of our results mainly comes from the linear fit of the temperature coefficients as shown in Table 1. The real interfacial thermal conductance at room temperature increases with increased layer number of MoS$_2$ from around 0.974 MWm^{-2}K^{-1} to 68.6 MWm^{-2}K^{-1}. The thermal conductance
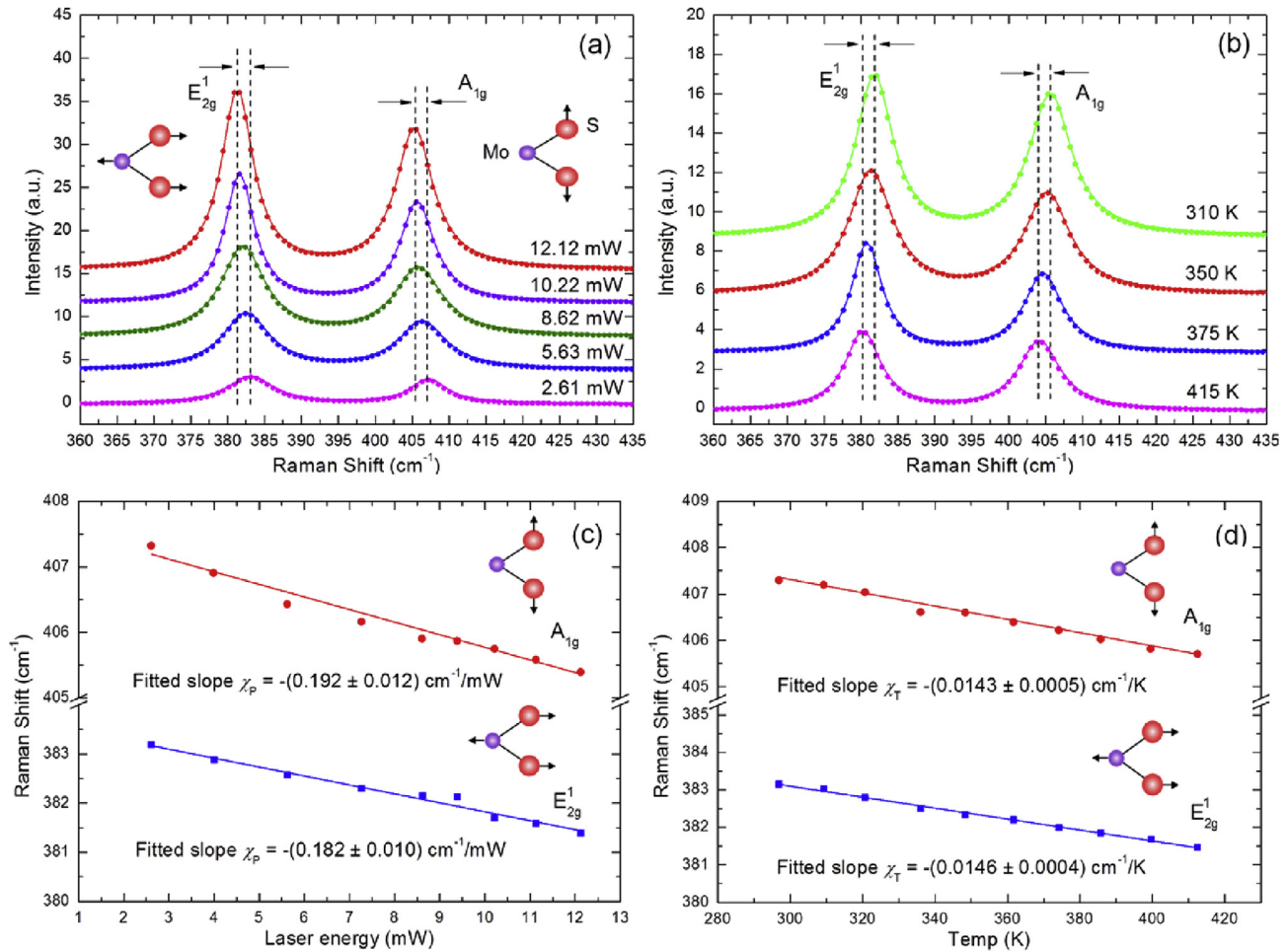
Fig. 4. The Lorentzian-fit Raman spectra of MoS$_2$ nanosheets. The sample with a thickness of 4.2 nm is used as example to illustrate the micro-Raman interfacial thermal conductance experiment and Raman temperature calibration results. (a) The Raman spectra of MoS$_2$ under increased excitation laser power in ambient environment. Spectra are shifted vertically to distinguish them. (b) The Raman spectra of MoS$_2$ collected at 310, 350, 375 and 415 K during Raman temperature coefficient calibration. (c) The Raman shift for A_{1g} (red circle) and E^1_{2g} (blue square) modes as a function of laser power during interfacial thermal conductance experiment. Fitting results (solid lines) for linear power coefficients χ_P are shown in the figure. (d) The Raman shift for A_{1g} (red circle) and E^1_{2g} (blue square) modes as a function of temperature in calibration experiment. Fitting results (solid lines) for linear temperature coefficients χ_T are shown in the figure. (For interpretation of the references to colour in this figure legend, the reader is referred to the web version of this article.)

increases by 70 times. They are almost on the same order of magnitude as the interfacial thermal conductance of monolayer graphene supported on SiO$_2$ [(28 + 16/−9.2) MW/m^{2}K] [33]. The interfacial thermal conductance of MoS$_2$ monolayer supported on SiO$_2$/Si substrates was found to vary from 1.94 MWm^{-2}K^{-1} at 300 K to 1.25 MWm^{-2}K^{-1} at 450 K [36]. This result is quite close to the interfacial thermal conductance we report here for the thin MoS$_2$ nanosheet (7 and 8 layers). The values are also similar to those reported for different metal-insulator interfaces which lies between 30 MWm^{-2}K^{-1} and 110 MWm^{-2}K^{-1}. The results deviation presumably reflects the relatively poor nature of interface prepared by the mechanical exfoliation process. The fact that thicker samples having a higher G_k in our work indicates their better surface contact with the substrate, leading to accordingly improved interfacial energy coupling. As we discussed before, the wrinkles and/or ripples could be introduced to the nanosheets during the mechanical exfoliation process. And the thinner MoS$_2$ nanosheet samples are softer and more likely to get folded and corrugated. For example, as shown in Fig. 1(f), there is a folded area just at the bottom the sample. All these mechanical-folding type defects could definitely decrease the interface thermal conductance. Tang et al.'s MD simulation results show that the thermal conductance at the

graphene-Si interface will decrease by 3 orders of magnitude when the spacing or separation between them increases by just about 0.3 nm [24]. The intrinsic value of the MoS$_2$/c-Si interfacial thermal conductance could be higher as shown in our molecular dynamics simulation discussed later in this work.

4.3. Variation of G_e against layer number: interpretation from interface structure

To further interpret our above interfacial thermal conductance results, we perform the following Raman intensity enhancement study to reveal the interface structure. If there is a tiny spacing between MoS$_2$ and c-Si at the interface, the local thermal conductance will reduce significantly. At the same time, the tiny spacing will give rise of Raman intensity. So in this section we study the Raman intensity of the MoS$_2$ sample against its thickness, in anticipation to uncover the local interface spacing information. The multiple reflection of the incident laser beam and Raman signal within a supported film and the spacing between it and the substrate has been studied in previous work [47,48]. The net absorption factor (F_{ab}) is given by
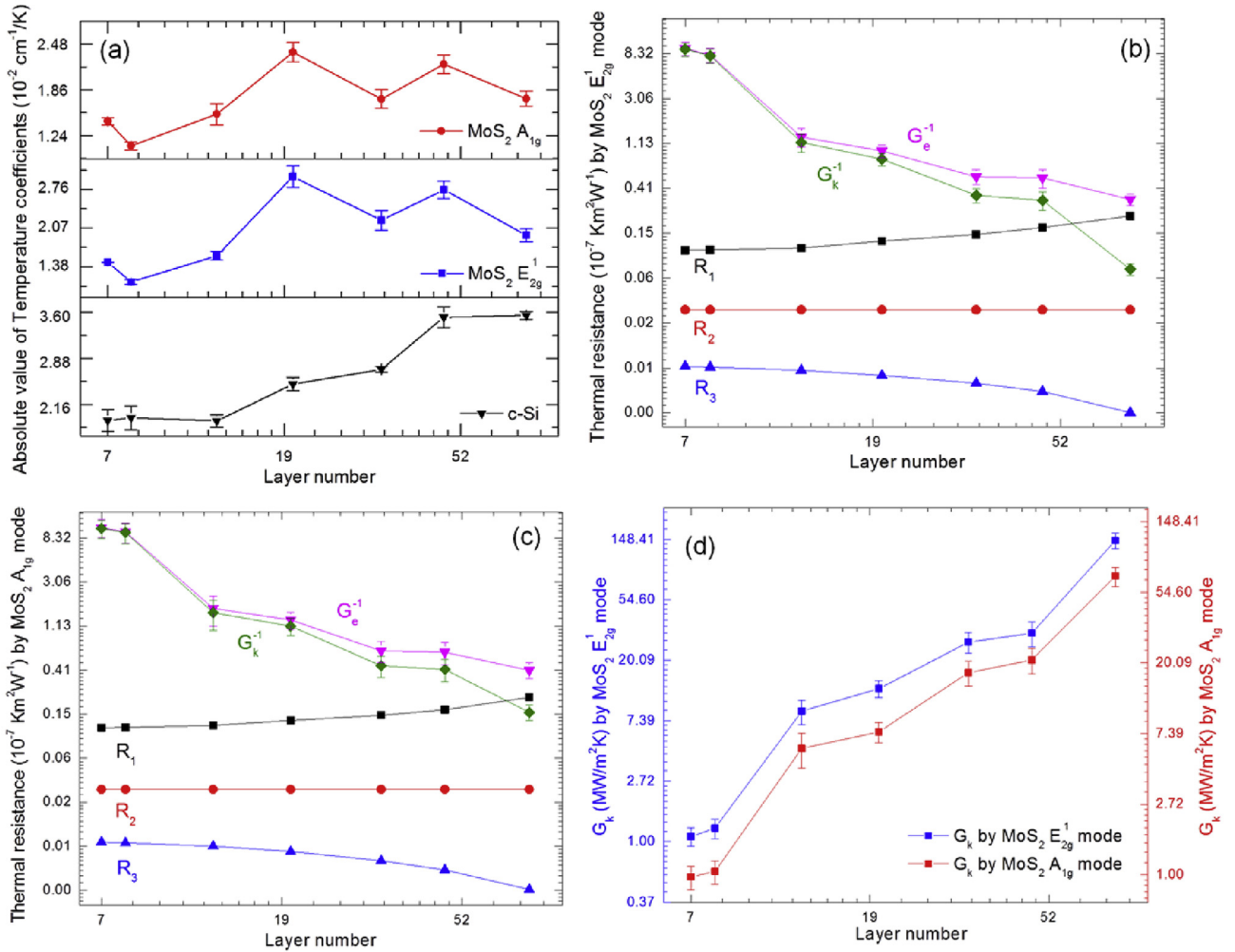
Fig. 5. (a) The temperature coefficients of the two MoS₂ vibration modes and c-Si for different layered MoS₂ samples. Thermal resistances R₁, R₂, and R₃ are compared with G_e^{-1} and G_k^{-1} obtained from the Raman parameters of MoS₂E_{2g}^1 mode (b) and A_{1g} mode (c). (d) Interfacial thermal conductance between different layered MoS₂ and c-Si based on Raman properties of both E_{2g}^1 and A_{1g} mode.

$$F_{ab} = t_1 \frac{\left(1 + r_2 r_3 e^{-2ib_2}\right)e^{-ib_x} + \left(r_2 + r_3 e^{-2ib_2}\right)e^{-i(b_1 - b_x)}}{1 + r_2 r_3 e^{-2ib_2} + \left(r_2 + r_3 e^{-2ib_2}\right)r_1 e^{-2ib_1}}, \quad (12)$$

where $t_1 = 2n_0/(n_0 + \tilde{n}_1)$, $r_1 = (n_0 - \tilde{n}_1)/(n_0 + \tilde{n}_1)$, $r_2 = (\tilde{n}_1 - \tilde{n}_2)/(\tilde{n}_1 + \tilde{n}_2)$, and $r_3 = (\tilde{n}_2 - \tilde{n}_3)/(\tilde{n}_2 + \tilde{n}_3)$ are Fresnel transmittance and reflection coefficients for the interface involving air (0), MoS₂ nanosheets (1), air (2), and Si (3). n_0, $\tilde{n}_1$, $\tilde{n}_2$ and $\tilde{n}_3$ are the refractive indices for air, MoS₂ nanosheets, air, and c-Si, respectively. $\beta_x = 2\pi x \tilde{n}_1/\lambda$, $\beta_1 = 2\pi d_1 \tilde{n}_1/\lambda$ and $\beta_2 = 2\pi d_2 \tilde{n}_2/\lambda$, where x is the depth of the point where interaction occurs, λ is the wavelength of incident laser, d_1 and d_2 are the thickness of MoS₂ nanosheets and c-Si, respectively. First of all, we assume there is no air between MoS₂ nanosheets and the c-Si substrate. The Raman intensity variation with the MoS₂ thickness will be compared with the experimental results to evaluate whether there is an interface spacing.

The net scattering factor (F_{sc}) is given by

$$F_{sc} = t_1' \frac{\left(1 + r_2 r_3 e^{-2ib_2}\right)e^{-ib_x} + \left(r_2 + r_3 e^{-2ib_2}\right)e^{-i(b_1 - b_x)}}{1 + r_2 r_3 e^{-2ib_2} + \left(r_2 + r_3 e^{-2ib_2}\right)r_1 e^{-2ib_1}}, \quad (13)$$

where $t_1' = 2\tilde{n}_1/(n_0 + \tilde{n}_1)$ and λ is the wavelength of the A_{1g} mode of MoS₂. Then the theoretical Raman intensity (F) is given as

$$F = \int_0^{d_1} |F_{ab} F_{sc}|^2 dx, \quad (14)$$

In the calculation, the refractive index of MoS₂ nanosheets is $5.2 - 1.1i$. The refractive indices of c-Si are $4.15 + 0.05i$ and $3.99 + 0.33i$ for incident laser and Raman scattering, respectively.

Fig. 6(a) shows the comparison of the experiment Raman peak intensity trend of MoS₂ A_{1g} mode and the theoretic Raman intensity F for our seven MoS₂ nanosheets samples. In the figure, we assume that there is no spacing for 75-layer MoS₂ sample for the theoretical Raman intensity calculation. The deviation of the calculation results and our experiment results uncovers the spacing existence for other six MoS₂ samples, especially for the thicker ones, 33 and 48-layer MoS₂. Compared with the theoretical calculation, Fig. 6(a) shows that when the MoS₂ becomes thinner, the experimental Raman intensity is much higher than the case without interface spacing. This strongly proves the existence of spacing between MoS₂ and c-Si. The spacing between the sample and its substrate will dramatically weaken the interatomic forces
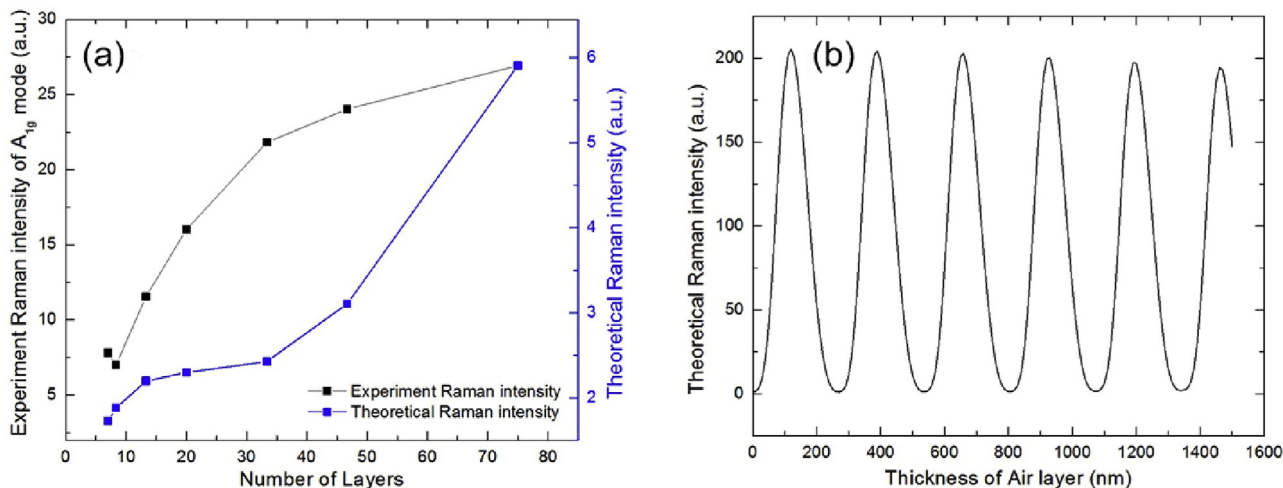
Fig. 6. (a) The comparison of the experiment Raman peak intensity trend of $MoS_2 A_{1g}$ mode and the theoretical Raman intensity F for our seven MoS_2 nanosheets samples. (b) Theoretical Raman intensity F as a function of the air layer thickness. For this case, the number of layers of MoS_2 takes 75.

between them. This will lower the thermal energy coupling between the MoS_2 and c-Si system. Eventually, the spacing will result in a much lower interfacial thermal conductance. To demonstrate how the interface spacing can change the Raman intensity, we take the 75-layer (45 nm) MoS_2 as an example to calculate how much the Raman intensity will change when the spacing thickness changes. This result is shown in Fig. 6(b). This possible loose contact could also result in the different temperature coefficients for different layered MoS_2 samples as shown in Fig. 5(a). Additionally, with the laser heating of the sample, imperfect contact between thick MoS_2 nanosheets and c-Si interface could more likely transform into relatively well smooth contact, leading to more effectively heat transfer.

5. Physics interpretation based on molecular dynamics simulations

To help better interpret the experimental results, molecular dynamics (MD) simulations are conducted to study the MoS_2/c-Si interfacial thermal conductance. The inset of Fig. 7(a) shows the physical domain construction for a MoS_2 nanosheet sample placed above a silicon bulk. There are nine layers of MoS_2 and it measures $17.7 \times 3.8 \times 5.2$ nm^3. The silicon bulk measures $22.3 \times 5.8 \times 5.3$ nm^3. Varshney et al. [49] have studied the force field of MoS_2 systematically. Following their work, we create an orthorhombic unit cell based on the original non-orthorhombic structure of MoS_2. This transformation does not change any modeling dynamics for its constituent atomic entities [49].

The set 8 of the force field parameter in the work of Varshney et al. [49] is used in this simulation. The bond interaction of Mo and S is described by the Morse interaction. The angle component of the force field is described by harmonic style. The non-bonded component of the force field is described by the Lennard-Jones (12-6) potential. The partial electrostatic charge of Mo is 0.76 and of S is -0.38 in the unit of one electron charge. Standard Ewald summation is employed to take care of the long-range Coulombic interaction. Table 2 shows the details of the force filed parameters for MoS_2. All simulations here were performed using LAMMPS molecular dynamics package from Sandia National Laboratories [50].

Since the interaction between the MoS_2 and c-Si is weak, the van

der Waals force and Lennard-Jones (12-6) potential are employed to describe the interaction. Similar method has been used for interface interaction of other materials [28,51–53]. According to the universal force field [54], the parameters of the Lennard-Jones potential are: σ_{S-Si}=3.71 Å, σ_{Mo-Si}=3.27 Å, ε_{S-Si}=0.0143 eV, ε_{Mo-Si}=0.0065 eV. The initial distance of MoS_2 and c-Si is set to be 3.54 Å. Periodic boundary condition is applied to the x and y (in-plane) directions and free boundary condition for the z (out-of-plane) direction. The conjugate gradient method is used for the initial minimization. The distance between MoS_2 and c-Si is 2.5 Å at equilibrium. Afterwards, MoS_2 is irradiated by a short thermal pulse of $q = 3.6 \times 10^{-3}$ W for 50 fs.

Because of the thermal pulse, the temperature of MoS_2 has an abrupt increase in the beginning. Then heat would be transported from MoS_2 nanosheets to c-Si. The temperature of MoS_2 decreases while the temperature of c-Si increases. Fig. 7(a) shows the temperature evolution of MoS_2 and c-Si for a 7-layered MoS_2 sheet. To precisely determine the interface thermal conductance, the top 4 layers of c-Si bulk are chosen for the temperature calculation, and the bottom 2 layers of MoS_2 are used for its temperature calculation. The interfacial thermal conductance is calculated as

$$G = -\frac{n \times C_p \times \partial T/\partial t}{\left[T|_{MoS_2} - T|_{Si} \right] \times A}, \tag{15}$$

where $\partial T/\partial t$ is the temperature changing rate of MoS_2. $T|_{MoS_2}$ is the bottom temperature of MoS_2, and $T|_{Si}$ is the surface temperature of c-Si. A is the contact area of MoS_2 and c-Si. n is the number of mole and C_p is heat capacity of the MoS_2 nanosheet. In our calculation, the average temperature of MoS_2 is first fitted with an exponential function first, then $\partial T/\partial t$ is calculated based on the fitted exponential function. For $T|_{MoS_2}$ and $T|_{Si}$, instead of using the raw data in Eq. (15), we first fit them using an exponential function, as shown in Fig. 7(a), and then use the fitted data for interface thermal conductance calculation. All these treatments are intended to reduce the statistical noise in the MD raw data.

Fig. 7(b) shows the interfacial thermal conductance determined from Eq. (15). The calculated G changes during thermal relaxation due to change of the energy coupling of the interface. The interface thermal conductance is roughly proportional to the interface materials phonon specific heat and the phonon
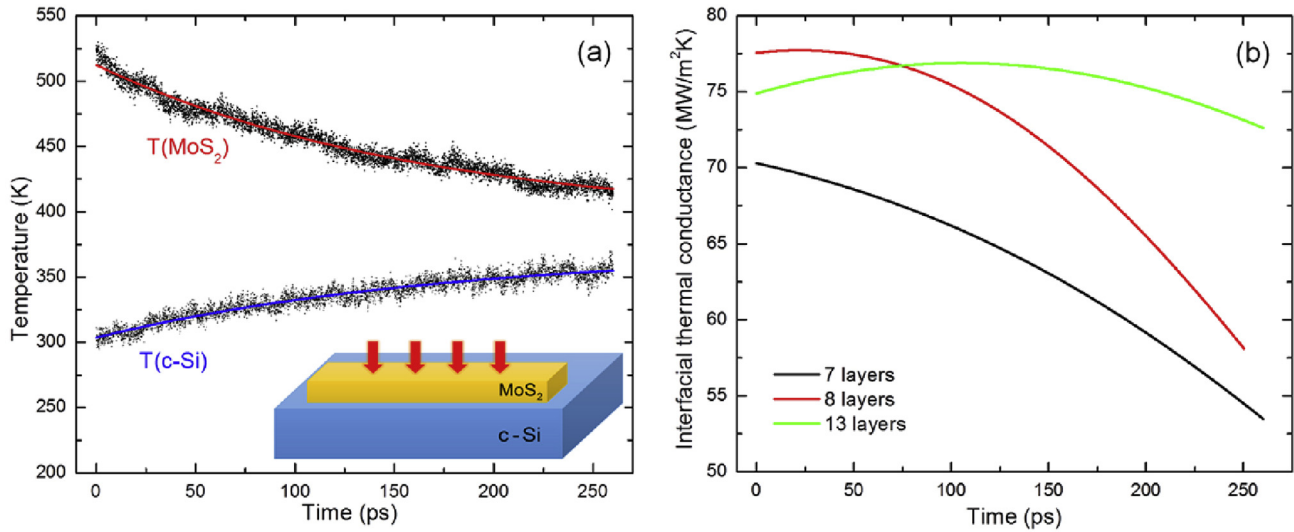
Fig. 7. (a) Temperature of c-Si and *MoS₂* of 7 layers during the thermal relaxation in MD simulation. The red curve shows the fitting of MoS₂ temperature: $T = 392 + 119 \times exp(-6.08 \times 10^{-3} \times t)$. The blue curve shows the fitting of c-Si surface temperature. The top 4 layers of c-Si bulk are chosen for the temperature calculation. The fitting result is $T = 370 - 66.8 \times exp(-5.65 \times 10^{-3} \times t)$. The inset shows the MD simulation Model configuration. MoS₂ is placed above c-Si which is of the size 22.3 × 5.8 × 5.3 nm³. The size of MoS₂ is 17.7 × 3.8 × 5.2 nm³. (b) Interfacial thermal conductance changes with the time for three MD cases: 7L, 8L, and 13L. Time 0 indicates the end time of laser irradiation. (For interpretation of the references to colour in this figure legend, the reader is referred to the web version of this article.)

Table 2
The force field parameters of MoS₂. The bond interaction between Mo and S is described by the Morse interaction. The angle component of the force field is described by harmonic style. The non-bonded component of the force field is described by the Lennard-Jones (12-6) potential. The metal unit is adopted in LAMMPS. Å is for distance and eV is for energy.

Parameters	Potential	Coefficients
Bond (Mo-S)	Morse interaction	$D_0 = 19.945$, $\alpha = 0.858$, $r_0 = 2.39$
Angle (Mo-S-Mo)	Harmonic style	$K = 2.5163$, $\theta_0 = 82$
Angle (S-Mo-S)	Harmonic style	$K = 2.5163$, $\theta_0 = 82$
Non-bonded (Mo-Mo)	Lennard-Jones (12-6)	$\varepsilon = 0.8382$, $\sigma = 2.551$
Non-bonded (S-S)	Lennard-Jones (12-6)	$\varepsilon = 0.0606$, $\sigma = 3.3695$
Non-bonded (Mo-S)	Lennard-Jones (12-6)	$\varepsilon = 0.0339$, $\sigma = 2.9318$
Equation for Morse interaction: $E = D_0[e^{-2\alpha(r-r_0)} - 2e^{-\alpha(r-r_0)}]$,		
Equation for Harmonic interaction: $E = K(\theta - \theta_0)^2$.		
Equation for Lennard-Jones (12-6): $E = 4\varepsilon[(\sigma/r)^{12} - (\sigma/r)^6]$.		

transmission [55]. During thermal relaxation, although the c-Si surface temperature increases a little bit, MoS₂ bottom temperature reduces more. Therefore, the interface material phonon specific heat goes down, leading to decreased G. More detailed explanation about the temperature effect on interface thermal conductance can be found in our recent work [55]. The thermal conductance is different for these three different cases. Generally speaking, we can conclude that when the material is thicker, the interface thermal conductance is higher. This trend agrees well with our experimental observation. In our MD simulation, we have tried thinner MoS₂ nanosheets, but found they are vulnerable to tiny stress in the material, and intend to warp. So the increased mechanical stiffness of thicker samples will help form a better contact with the c-Si substrate, leading to increased interface thermal conductance. Based on the results shown in Fig. 7(b), we could get the interfacial thermal conductance around 56.6, 62.0, and 74.1 MWm⁻² K⁻¹ for 7L, 8L, and 13L respectively. These are higher than the experiment result (Table 1) of respectively layered MoS₂. This reveals the imperfect contact of MoS₂ and c-Si in our experiments samples. The upper bound of our experimentally measured G is 68.6 ± 9.14 MWm⁻²K⁻¹, very close to the MD simulation result.

6. Conclusion

In this work, we measured the interfacial thermal conductance (G) between few to tens of layered MoS₂ and c-Si substrate. It was found G increased with increasing layers of MoS₂ from approximately 0.974 MWm⁻²K⁻¹ for 7 layers to 68.6 MWm⁻²K⁻¹ for around 75 layers at room temperature. This close-to-two order of magnitude change in G reflected the interface spacing change versus the MoS₂ thickness. To better identify the morphology of MoS₂/c-Si interface, the interference enhancement of Raman signal of MoS₂ nanosheets was studied to confirm the spacing variation. The experimental Raman intensity was significantly higher than that of tight MoS₂-Si contact, uncovering the strong interface optical interference and the local spacing. To further understand the experimental results, we have conducted MD simulations to calculate the interface thermal conductance between MoS₂ and c-Si. It showed that thicker samples have a higher G, similar to the experimental observation. This could be explained by the improved mechanical stiffness of thicker samples and the resulting better interface contact. For the all the three samples under study (7, 8, and 13 layered), their G shows a decreasing trend against the local temperature. This was explained by the reduced phonon specific heat against decreased temperature. The calculated G agreed well

P. Yuan et al. / Acta Materialia 122 (2017) 152–165

with the upper bound *G* observed in our experiment, indicating when MoS$_2$ is thick (tens of nm), the local interface is close to the ideal scenario determined by local van der Waals bonding. Future work on thickness control of the sample will be conducted to investigate interface thermal conductance variation for each thickness level of the sample.

Acknowledgements

References

[1] A.P. Gaur, S. Sahoo, M. Ahmadi, S.P. Dash, M.J.-F. Guinel, R.S. Katiyar, Surface energy engineering for tunable wettability through controlled synthesis of MoS2, Nano Lett. 14 (2014) 4314–4321.

[2] A.P. Gaur, S. Sahoo, M. Ahmadi, M.J.-F. Guinel, S.K. Gupta, R. Pandey, S.K. Dey, R.S. Katiyar, Optical and vibrational studies of partially edge-terminated vertically aligned nanocrystalline MoS2 thin films, J. Phys. Chem. C 117 (2013) 26262–26268.

[3] Q.H. Wang, K. Kalantar-Zadeh, A. Kis, J.N. Coleman, M.S. Strano, Electronics and optoelectronics of two-dimensional transition metal dichalcogenides, Nat. Nanotechnol. 7 (2012) 699–712.

[4] U. Ahuja, A. Dashora, Electronic and Optical Properties of MoS2. Solid State Phenomena, vol. 209, Trans Tech Publ, 2014, pp. p.90–93.

[5] J. Hu, J. Zabinski, Nanotribology and lubrication mechanisms of inorganic fullerene-like MoS2 nanoparticles investigated using lateral force microscopy (LFM), Tribol. Lett. 18 (2005) 173–180.

[6] K. Chang, W. Chen, L-cysteine-assisted synthesis of layered MoS2/graphene composites with excellent electrochemical performances for lithium ion batteries, ACS Nano 5 (2011) 4720–4728.

[7] O. Lopez-Sanchez, D. Lembke, M. Kayci, A. Radenovic, A. Kis, Ultrasensitive photodetectors based on monolayer MoS2, Nat. Nanotechnol. 8 (2013) 497–501.

[8] S. Bertolazzi, D. Krasnozhon, A. Kis, Nonvolatile memory cells based on MoS2/graphene heterostructures, ACS Nano 7 (2013) 3246–3252.

[9] S. Kim, A. Konar, W.-S. Hwang, J.H. Lee, J. Lee, J. Yang, C. Jung, H. Kim, J.-B. Yoo, J.-Y. Choi, High-mobility and low-power thin-film transistors based on multilayer MoS2 crystals, Nat. Commun. 3 (2012) 1011.

[10] M. Freitag, M. Steiner, Y. Martin, V. Perebeinos, Z. Chen, J.C. Tsang, P. Avouris, Energy dissipation in graphene field-effect transistors, Nano Lett. 9 (2009) 1883–1888.

[11] M. Schulz, Thermal interface: a key factor in improving lifetime in power electronics, in: Power Conversion and Intelligent Motion Conference, 2012.

[12] P. Blazdell. Basics of Thermal Management Materials for Micro-electronics—theory and practise.

[13] P. Kapitza, The study of heat transfer in helium II, J. Phys. USSR 4 (1941) 181–210.

[14] J. Robertson, Interfaces and defects of high-K oxides on silicon, Solid-State Electron. 49 (2005) 283–293.

[15] A. Ziegler, J.C. Idrobo, M.K. Cinibulk, C. Kisielowski, N.D. Browning, R.O. Ritchie, Interface structure and atomic bonding characteristics in silicon nitride ceramics, Science 306 (2004) 1768–1770.

[16] P.E. Hopkins, Thermal transport across solid interfaces with nanoscale imperfections: effects of roughness, disorder, dislocations, and bonding on thermal boundary conductance, ISRN Mech. Eng. 2013 (2013).

[17] R.J. Stevens, L.V. Zhigilei, P.M. Norris, Effects of temperature and disorder on thermal boundary conductance at solid–solid interfaces: nonequilibrium molecular dynamics simulations, Int. J. Heat Mass Transf. 50 (2007) 3977–3989.

[18] P.E. Hopkins, L.M. Phinney, J.R. Serrano, T.E. Beechem, Effects of surface roughness and oxide layer on the thermal boundary conductance at aluminum/silicon interfaces, in: 2010 14th International Heat Transfer Conference: American Society of Mechanical Engineers, 2010, pp. 313–319.

[19] V. Casalegno, P. Vavassori, M. Valle, M. Ferraris, M. Salvo, G. Pintsuk, Measurement of thermal properties of a ceramic/metal joint by laser flash method, J. Nucl. Mater. 407 (2010) 83–87.

[20] G. Pernot, M. Stoffel, I. Savic, F. Pezzoli, P. Chen, G. Savelli, A. Jacquot, J. Schumann, U. Denker, I. Mönch, Precise control of thermal conductivity at the nanoscale through individual phonon-scattering barriers, Nat. Mater. 9 (2010) 491–495.

[21] B.C. Gundrum, D.G. Cahill, R.S. Averback, Thermal conductance of metal-metal interfaces, Phys. Rev. B 72 (2005) 245426.

[22] D.G. Cahill, K. Goodson, A. Majumdar, Thermometry and thermal transport in micro/nanoscale solid-state devices and structures, J. Heat Transf. 124 (2002) 223–241.

[23] Y. Yue, J. Zhang, X. Wang, Micro/Nanoscale spatial resolution temperature probing for the interfacial thermal characterization of epitaxial graphene on 4H-SiC, Small 7 (2011) 3324–3333.

[24] X. Tang, S. Xu, J. Zhang, X. Wang, Five orders of magnitude reduction in energy coupling across corrugated graphene/substrate interfaces, ACS Appl. Mater. Interfaces 6 (2014) 2809–2818.

[25] J. Diao, D. Srivastava, M. Menon, Molecular dynamics simulations of carbon nanotube/silicon interfacial thermal conductance, J. Chem. Phys. 128 (2008) 164708.

[26] M. Hu, P. Keblinski, P.K. Schelling, Kapitza conductance of silicon–amorphous polyethylene interfaces by molecular dynamics simulations, Phys. Rev. B 79 (2009) 104305.

[27] H. Zhong, J.R. Lukes, Interfacial thermal resistance between carbon nanotubes: molecular dynamics simulations and analytical thermal modeling, Phys. Rev. B 74 (2006) 125403.

[28] J. Zhang, Y. Wang, X. Wang, Rough contact is not always bad for interfacial energy coupling, Nanoscale 5 (2013) 11598–11603.

[29] R. Prasher, Acoustic mismatch model for thermal contact resistance of van der Waals contacts, Appl. Phys. Lett. 94 (2009) 1905.

[30] W. Little, The transport of heat between dissimilar solids at low temperatures, Can. J. Phys. 37 (1959) 334–349.

[31] P. Reddy, K. Castelino, A. Majumdar, Diffuse mismatch model of thermal boundary conductance using exact phonon dispersion, Appl. Phys. Lett. 87 (2005) 211908.

[32] B. Persson, H. Ueba, Heat transfer between weakly coupled systems: graphene on a-SiO2, EPL Europhys. Lett. 91 (2010) 56001.

[33] W. Cai, A.L. Moore, Y. Zhu, X. Li, S. Chen, L. Shi, R.S. Ruoff, Thermal transport in suspended and supported monolayer graphene grown by chemical vapor deposition, Nano Lett. 10 (2010) 1645–1651.

[34] K.F. Mak, C.H. Lui, T.F. Heinz, Measurement of the thermal conductance of the graphene/SiO2 interface, Appl. Phys. Lett. 97 (2010) 221904.

[35] Z. Chen, W. Jang, W. Bao, C. Lau, C. Dames, Thermal contact resistance between graphene and silicon dioxide, Appl. Phys. Lett. 95 (2009) 161910.

[36] A. Taube, J. Judek, A. Łapinska, M. Zdrojek, Temperature-dependent thermal properties of supported MoS2 monolayers, ACS Appl. Mater. Interfaces 7 (2015) 5061–5065.

[37] H. Li, J. Wu, Z. Yin, H. Zhang, Preparation and applications of mechanically exfoliated single-layer and multilayer MoS(2) and WSe(2) nanosheets, Acc. Chem. Res. 47 (2014) 1067–1075.

[38] M.A. Meitl, Z.-T. Zhu, V. Kumar, K.J. Lee, X. Feng, Y.Y. Huang, I. Adesida, R.G. Nuzzo, J.A. Rogers, Transfer printing by kinetic control of adhesion to an elastomeric stamp, Nat. Mater. 5 (2006) 33–38.

[39] P. Nemes-Incze, Z. Osváth, K. Kamarás, L. Biró, Anomalies in thickness measurements of graphene and few layer graphite crystals by tapping mode atomic force microscopy, Carbon 46 (2008) 1435–1442.

[40] E.X. Perez, Design, Fabrication and Characterization of Porous Silicon Multilayer Optical Devices, Departament d'Enginyeria Electrònica, Elèctrica i Automàtica, vol. Doctoral: Universitat Rovira i Virgili, 2007.

[41] H. Zhang, Y. Ma, Y. Wan, X. Rong, Z. Xie, W. Wang, L. Dai, Measuring the refractive index of highly crystalline monolayer MoS2 with high confidence, Sci. Rep. 5 (2015).

[42] S. Sahoo, A.P. Gaur, M. Ahmadi, M.J.-F. Guinel, R.S. Katiyar, Temperature-dependent Raman studies and thermal conductivity of few-layer MoS2, J. Phys. Chem. C 117 (2013) 9042–9047.

[43] J. Liu, G.-M. Choi, D.G. Cahill, Measurement of the anisotropic thermal conductivity of molybdenum disulfide by the time-resolved magneto-optic Kerr effect, J. Appl. Phys. 116 (2014) 233107.

[44] C. Lee, H. Yan, L.E. Brus, T.F. Heinz, J. Hone, S. Ryu, Anomalous lattice vibrations of single-and few-layer MoS2, ACS Nano 4 (2010) 2695–2700.

[45] L. Su, Y. Zhang, Y. Yu, L. Cao, Dependence of coupling of quasi 2-D MoS 2 with substrates on substrate types, probed by temperature dependent Raman scattering, Nanoscale 6 (2014) 4920–4927.

[46] T. Beechem, S. Graham, S.P. Kearney, L.M. Phinney, J.R. Serrano, Invited Article: simultaneous mapping of temperature and stress in microdevices using micro-Raman spectroscopy, Rev. Sci. Instrum. 78 (2007) 061301.

[47] Y. Wang, Z. Ni, Z. Shen, H. Wang, Y. Wu, Interference enhancement of Raman signal of graphene, arXiv Prepr. arXiv:0801 4595 (2008).

[48] D. Yoon, H. Moon, Y.-W. Son, J.S. Choi, B.H. Park, Y.H. Cha, Y.D. Kim, H. Cheong, Interference effect on Raman spectrum of graphene on SiO 2/Si, Phys. Rev. B 80 (2009) 125422.

[49] V. Varshney, S.S. Patnaik, C. Muratore, A.K. Roy, A.A. Voevodin, B.L. Farmer, MD simulations of molybdenum disulphide (MoS2): force-field parameterization and thermal transport behavior, Comput. Mater. Sci. 48 (2010) 101–108.

[50] S. Plimpton, Fast parallel algorithms for short-range molecular dynamics, J. Comput. Phys. 117 (1995) 1–19.

[51] J. Xiao, S. Dunham, P. Liu, Y. Zhang, C. Kocabas, L. Moh, Y. Huang, K.-C. Hwang, C. Lu, W. Huang, J.A. Rogers, Alignment controlled growth of single-walled carbon nanotubes on quartz substrates, Nano Lett. 9 (2009) 4311–4319.

[52] Z.-Y. Ong, E. Pop, Molecular dynamics simulation of thermal boundary conductance between carbon nanotubes and SiO2, Phys. Rev. B 81 (2010).

[53] S.-W. Chang, A.K. Nair, M.J. Buehler, Geometry and temperature effects of the interfacial thermal conductance in copper– and nickel–graphene nano-composites, J. Phys. Condens. Matter 24 (2012) 245301.

[54] A.K. Rappe, C.J. Casewit, K.S. Colwell, W.A. Goddard, W.M. Skiff, UFF, a full periodic table force field for molecular mechanics and molecular dynamics simulations, J. Am. Chem. Soc. 114 (1992) 10024–10035.

[55] J. Liu, Z. Xu, Z. Cheng, S. Xu, X. Wang, Thermal conductivity of ultrahigh molecular weight polyethylene crystal: defect effect uncovered by 0 K limit phonon diffusion, ACS Appl. Mater. Interfaces 7 (2015) 27279–27288.